Supplementary Information

Many-body van der Waals interactions in multilayer structures studied by atomic force microscopy

Xiao Wang[1#], Zepu Kou[1#], Ruixi Qiao[2], Yuyang Long[1], Baowen Li[1], Xuemei Li[1,3], Wanlin Guo[1,2], Xiaofei Liu*[1], Jun Yin*[1]

[1]State Key Laboratory of Mechanics and Control for Aerospace Structures, Key Laboratory for Intelligent Nano Materials and Devices of the Ministry of Education, Nanjing University of Aeronautics and Astronautics, Nanjing, 210016, P. R. China.

[2]Institute for Frontier Science, Nanjing University of Aeronautics and Astronautics, Nanjing, 210016, P. R. China.

[3]College of Material Science and Engineering, Nanjing University of Aeronautics and Astronautics, Nanjing, 210016, P. R. China.

Email: liuxiaofei@nuaa.edu.cn, yinjun@nuaa.edu.cn

Contents

Supplementary Note 1. Samples characterization

Raman characterization. The graphene was transferred onto the SiO_2 for Raman characterization using 532 nm laser. Supplementary Fig. 3 displays the typical Raman spectra of CVD graphene and suspended graphene. The absence of *D* peak around 1350 cm^{-1} suggests the high quality of all samples. The full width at half maximum (FWHM) of 2*D* peak is in the range of 27.5 ± 3.8 cm^{-1}, confirming that all samples are monolayer[1].

Supplementary Note 2. Removing surface contaminants of graphene

To verify the efficiency of thermal annealing in removing the airborne contaminants, attenuated total reflection Fourier transform infrared (ATR-FTIR) spectroscopy was conducted before and after the vacuum thermal annealing, as shown in Supplementary Fig. 4. The results confirm that annealing at 200 °C for 1 h can efficiently remove hydrocarbon contaminants. The remaining, but notably weakened, peaks corresponding to $-CH_2$ and $-CH_3$ group maybe contribute to the unavoidable adsorption of the hydrocarbon due to the re-exposure to air during ATR-FTIR tests.

Besides the thermal annealing, contact mode imaging of the target region at large normal loads was also performed to further remove the hydrocarbon residuals, if there is any[2]. Similarly, any residual PMMA on suspended sample can be efficiently removed through this method.

Supplementary Note 3.1. Dynamic force curves in frequency modulation AFM

As shown in Supplementary Fig. 5, we acquired the force spectrum between an AFM tip and mono@Cu by frequency modulation (FM) AFM. The deduced force curve by Sader-Jarvis method[3] (Supplementary Fig. 5b) cannot be well described by $F = RH/6d^2$, which is commonly adapted for describing the sphere-plane vdW interaction. Here, R is the radius of tip, H is the Hamaker constant, d is the distance of closest approach between surfaces. The force field of the multilayer system investigated here is expected to be different from that well established for two homogeneous bodies.

During the FM-AFM measurements, the spring constants of cantilever (~160 N/m, BL-AC55TS) and inverse optical lever sensitivity of system were calibrated by the thermal noise and Sader methods, respectively. The tip approaches the sample with a velocity of 1 nm/s and a vibration amplitude of 1.5 nm. The first-order resonant frequency of the cantilever is ~ 2.2 MHz with a quality factor of 910. The measurements were conducted in N_2 environment to prevent the influence of water capillary and airborne contamination.

Due to the challenge in quantitative interpretation of the force-distance relationship for such multilayer systems, we focus on investigating the critical adhesion force in this work. In contrast, obtaining the critical adhesion force from dynamic force spectrum require a full-range integration of the force spectrum before the contact between tip and sample, following implicit functions with a critical approximation[3,4]. Such integration process may lead to accumulation of the test errors and large variation of the deduced adhesion force. We also determined the critical adhesion force through FM-AFM, and the results are summarized in Supplementary Fig. 5c. The deduced $P_{mono@Cu}/P_{bulk}$ ratio through FM-AFM ranges from 1.06 to 1.21, showing a significant larger variation compared with that determined by the quasi-static force curves.

Supplementary Note 3.2. Analysis of quasi-static force curves

To determine the adhesion force with a high accuracy, soft AFM cantilevers with an elastic constant (k_c) close to 0.2 N/m were adapted. At loading stage, once the force gradient of sample-tip (dF/dD) was greater than elastic constant of the cantilever, the tip snap-to-contact with the sample. As illustrated in Supplementary Fig. 6b, the cantilever destabilized at 6 nm away from the sample surface. The force signal detected BEFORE the snap-to-contact is comparable to the noise level. The ~1 nN force is the force experienced by the tip AFTER the snap-to-contact. The potential difference in

attractive force before the snap-to-contact is easily lost in the ±0.03 nN system force noise, which can be extracted from the force curve far away from contact as shown in Supplementary Fig. 6c.

The underestimation of adhesion force due to surface roughness is an important issue, and experiments have shown that the tip-sample adhesion shows an exponential decay with roughness[5,6]. The classical Rabinovich model[7], You's model[8] and Sun's model[9] have theoretically derived the effect of sample surface roughness on tip-sample adhesion. We plotted the normalized adhesion force vs. surface roughness of mono@Au samples predicted by these models in Supplementary Fig. 10c. It is common in all these models that ~ 0.4 nm surface roughness of the mono@Au sample leads to a reduction in the tip-sample adhesion force, although the reduction ratio varies greatly between models. Thus, we focused on the CVD grown mono@Cu samples in the manuscript, which are of atomically flat surface similar to that of graphite (Supplementary Fig. 1).

Supplementary Note 4.1. Details of the semiempirical pairwise vdW correction

As has been reported previously[10], the accurate C_6 coefficients for bulk or two-dimensional materials can differ from the free atom values. To improve the accuracy of the pairwise vdW correction, the C_6 coefficient of graphene derived by the vdW^{2D} method[11] and the C_6 coefficient of sp^3 Si derived by Zhang *et al.*[12] were applied. The experimental dielectric spectrum of Cu[13,14] was applied to calculate the frequency-dependent polarizability via the Clausius-Mossotti relation for bulk material,

$$\alpha(\omega) = \frac{3V}{4\pi} \cdot \frac{\varepsilon(\omega) - 1}{\varepsilon(\omega) + 2}, \tag{S1}$$

The C_6 coefficient of Cu was derived from its polarizability via the Casimir-Polder integral

$$C_6 = \frac{3}{\pi} \int_0^\infty \alpha(i\xi)\alpha(i\xi) d\xi, \tag{S2}$$

The derived C_6 coefficients take account of the effects of chemical bonding and dipole-dipole screening within each material[11], thus providing an improved description of interlayer interaction. The C_6 coefficients used in the pairwise vdW correction are listed in Supplementary Table 1, in comparison with the corresponding free atoms.

The vdW energy is calculated as the summation of interatomic pairwise potentials damped at short distance[10,11]

$$E_{\mathrm{vdW}} = -\frac{1}{2} \sum_{A,B} f_{\mathrm{damp}}(R^{AB}, R_0^A, R_0^B) C_6^{AB} (R^{AB})^{-6}, \tag{S3}$$

where R^{AB} is the distance between atoms A and B, C_6^{AB} is the atomic vdW coefficient, and R_0^A and R_0^B are the effective vdW radii, respectively. The coefficient for two different atoms C_6^{AB} is calculated from the derived C_6 coefficients of atoms A and B[10]

$$C_6^{AB} = \frac{2C_6^{AA} C_6^{BB}}{\frac{\alpha_B}{\alpha_A} C_6^{AA} + \frac{\alpha_A}{\alpha_B} C_6^{BB}}, \tag{S4}$$

where α_{A} and α_{B} are the static polarizability of atoms A and B, respectively. The damping function f_{damp} cutting off the short-range interaction reads[10]

$$f_{\mathrm{damp}}(R^{AB}, R_0^A, R_0^B) = \left\{ 1 + \exp\left[-d\left(\frac{R_{AB}}{s_R R_{AB}^0} - 1 \right) \right] \right\}^{-1}, \tag{S5}$$

Supplementary Note 4.2. Details of the many-body dispersion (MBD) theory

In the MBD framework, the long-range correlation energy E_{vdW}^{LR} is calculated via the coupled fluctuating dipole model. The Hamiltonian of MBD is defined as[15]

$$H_{MBD} = -\frac{1}{2}\sum_{p=1}^{N}\nabla_{d_p}^2 + \frac{1}{2}\sum_{p=1}^{N}\omega_p^2 d_p^2 + \sum_{p>q}^{N}\omega_p\omega_q\sqrt{\alpha_p^0\alpha_q^0}\,d_p\mathbf{T}_{pq}d_q, \tag{S6}$$

where ω_{p} and α_p^0 are static dipole polarizability and characteristic excitation frequency of atom p, respectively. d_p represents displacement of atom p from its equilibrium position R_p. The dipole-dipole interaction tensor between atoms p and q is $\mathbf{T}_{pq} = \nabla_{\mathbf{R}_p} \otimes \nabla_{\mathbf{R}_q} v(|\mathbf{R}_p - \mathbf{R}_q|)$. The MBD energy is then computed as the difference between the zero-point energies of interacting and noninteracting systems[16]

$$E_{\mathrm{vdW}}^{LR} = \frac{\hbar}{2}\sum_{i=1}^{3N}\bar{\omega}_i - \frac{3\hbar}{2}\sum_{j=1}^{N}\omega_j, \tag{S7}$$

where $\bar{\omega}_i$is the Hamiltonian eigenvalues and ω_j is eigen frequency of atom j.

Supplementary Note 5. Details of the Lifshitz theory calculations

To further provide a qualitative understanding of the many-body effect, the vdW interaction between the Si plate and the Cu-supported graphene was also investigated using the Lifshitz theory. To properly apply the Lifshitz theory, it is crucial to carefully define the electromagnetic boundaries, since a continuum medium approximation must be applied. As illustrated in Supplementary Fig. 14, graphene was considered as a continuum slab with a thickness of 3.3 Å, while a semi-infinite Cu substrate and a semi-infinite Si were adopted. The separation between the bottom surface of the graphene slab and the Cu substrate was set to be 1.65 Å, since the separation between the carbon plane and Cu surface is approximately 3.3 Å[17]. Dielectric functions taken from previous literatures[13,18,19] were applied. The detailed geometric parameters are labeled in Supplementary Fig. 14.

The vdW energy between a semi-infinite Si and Cu-supported monolayer graphene reads

$$E_{Si-\mathrm{mono}@Cu} = \frac{k_B T}{8\pi d^2} {\sum_{n=0}^{\infty}}' \int_{r_n}^{\infty} x \ln(1-\bar{\Delta}_{Si-vac1}\bar{\Delta}^{eff}_{mono-vac1}e^{-x})dx, \tag{S8}$$

where k_B and T are the Boltzmann constant and temperature. The Matsubara frequency ξ_n can be $\frac{2\pi n k_B T}{\hbar}$ with n being a non-negative integer and $\hbar$ being Planck's constant. The prime symbol on the summation sign means that the zero-frequency term is multiplied by 1/2. x in the integrand represents the modulus of in-plane wave vector. The Fresnel coefficient at the interface between Si and vacuum is

$$\bar{\Delta}_{Si-vac1} = \frac{x\varepsilon_{Si} - x_{Si}\varepsilon_{vac}}{x\varepsilon_{Si} + x_{Si}\varepsilon_{vac}}, \tag{S9}$$

where $x_{Si}^2 = x^2 + \left(2d\xi_n/c\right)^2\left(\varepsilon_{Si} - \varepsilon_{vac}\right)$. The detailed procedure for obtaining the effective Fresnel coefficient at the interface between graphene and vacuum $\bar{\Delta}^{eff}_{mono-vac1}$ can be found in the literature[20] or Adrian Parsegian's textbook[21]. The two-body vdW energy between Si and monolayer graphene $E_{Si\text{-}mono}$ (between Si and Cu, $E_{Si\text{-}Cu}$) was calculated in the corresponding bilayer without the third layer.

Supplementary Fig. 15 shows the ratio of the summation of two-body energies, $E_{Si\text{-}mono}+E_{Si\text{-}Cu}$, to the energy between Si and Cu-supported graphene, $E_{Si\text{-}mono@Cu}$. In the distance range from 5 to 200 Å, $E_{Si\text{-}mono}+E_{Si\text{-}Cu}$ is about 4%~14% larger than $E_{Si\text{-}mono@Cu}$, verifying again the many-body effect or the vdW screening effect in the trilayer. We

note that, as detailed atomic structures and nonlocal dielectric properties are neglected by the continuum models, the Lifshitz theory is more suitable for a qualitative understanding instead of a quantitative description of systems with atomic scale feature sizes/separations.

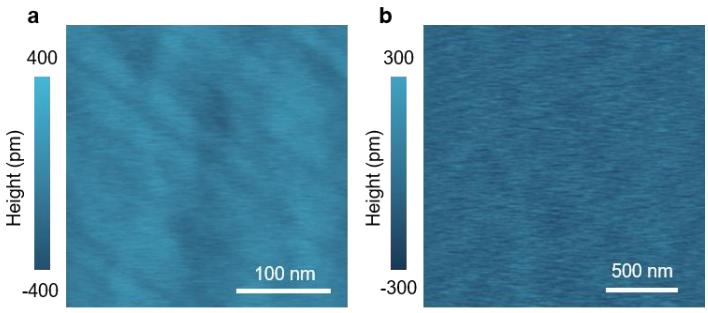

Supplementary Figure 1. Surface roughness of the samples.
a, b, The topography image of graphene on Cu (**a**) and bulk graphite (**b**). The roughness is around 70-80 pm for both the samples.

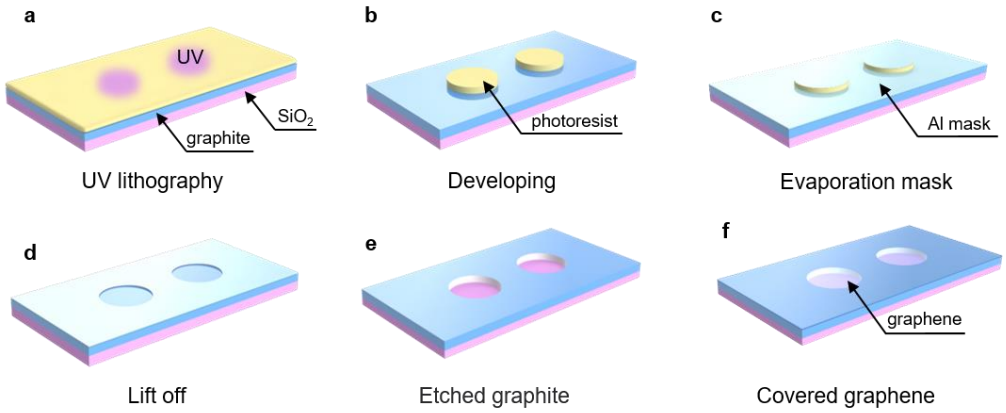

Supplementary Figure 2. Schematic of the fabrication process of suspended graphene devices.
a, The schematic of UV lithography using the negative property of AZ 5214E photoresist, and the developed sample as shown in **b. c,** Al film is deposited on sample surface as a mask, and then the cured photoresist was lifted off to expose the graphite as shown in **d**. **e,** The Al mask is removed and reactive ion etching is used to drill the graphite micro-holes. **f,** The suspended graphene is covered over the hole.

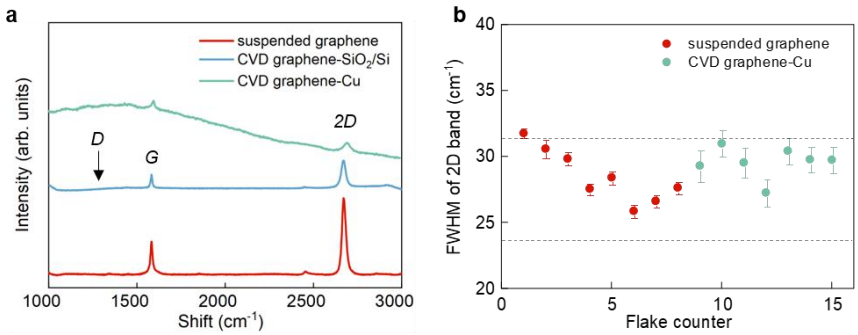

Supplementary Figure 3. The Raman spectrum of CVD graphene and suspended graphene. **a,** Spectrum of free-standing graphene, CVD graphene transferred onto SiO_2/Si substrate and CVD graphene on Cu. **b,** The full width at half maximum (FWHM) of 2*D* peak. Error bars represent the mean deviation.

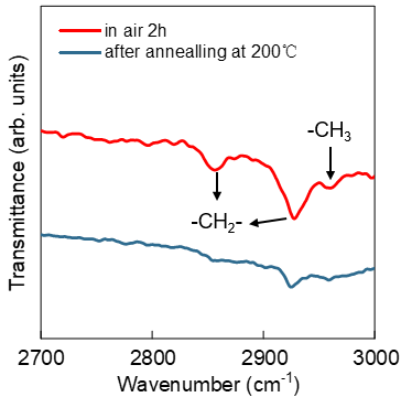

Supplementary Figure 4. Surface cleanness of graphene surface.
ATR-FTIR spectrum of graphene on Cu sample. The peaks at 2850 cm^{-1}, 2930 cm^{-1} and 2950^{-1} are assigned to the symmetric and asymmetry stretching of the -CH_2- group and asymmetric stretching of -CH_3 group, respectively.

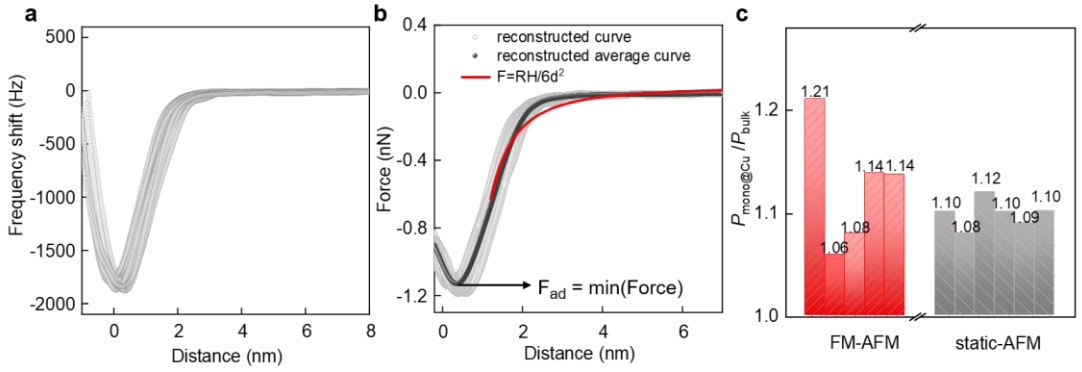

Supplementary Figure 5. Force curves obtained from FM-AFM.

a, Frequency shift versus distance curves obtained from the FM-AFM. **b,** Reconstructed force versus distance curves using Sader-Jarvis method. **c,** Ratios of critical adhesion force of the mono@Cu to that of the bulk graphite measured through FM-AFM (red bars) and static-AFM (gray bars). Each value is obtained through Gaussian fitting of more than 400 data of $P_{\text{mono@Cu}}/P_{\text{bulk}}$.

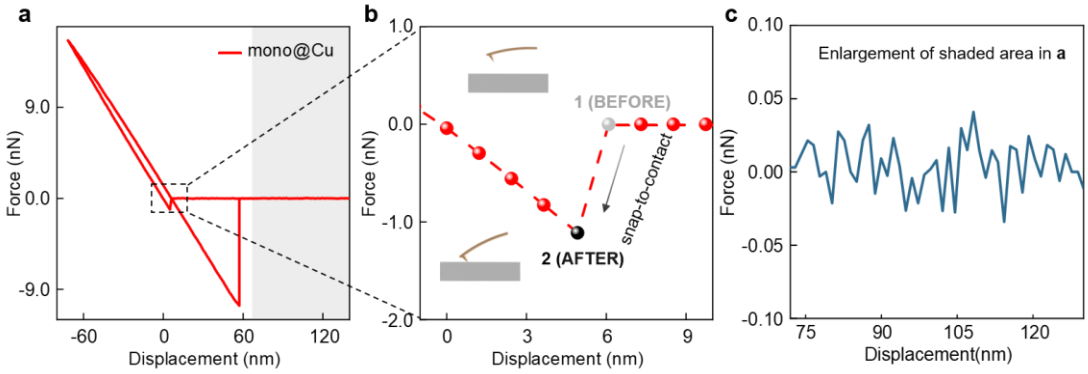

Supplementary Figure 6. Analysis force versus displacement curve.

a, Typical force versus displacement curve. **b,** The enlarged view to highlight the snap-to-contact process at the loading stage. 1 and 2 points represent the two states before and after snap-to-contact, corresponding cantilever schemes are shown at the top and bottom of **b**, respectively. **c,** The enlarged view of the shaded region in **a** to show the measurement noise.

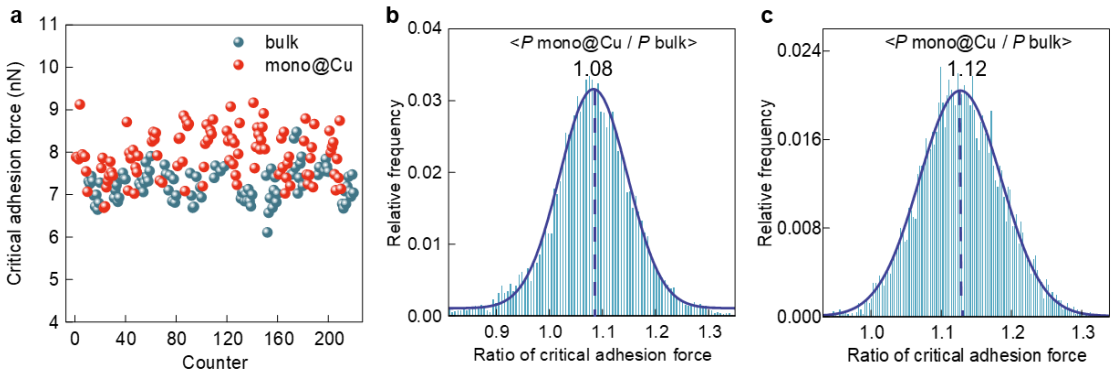

Supplementary Figure 7. The stability of force measurements using silicon tips.

a, Raw data of critical adhesive force detected on mono@Cu (red balls) and bulk graphite (blue balls). Stability in the adhesive force indicates the stability in tip topography. **b, c,** Histograms distribution of the ratio of $P_{mono@Cu}/P_{bulk}$. The solid lines are Gaussian fits. The standard deviations are 0.064 and 0.058, respectively.

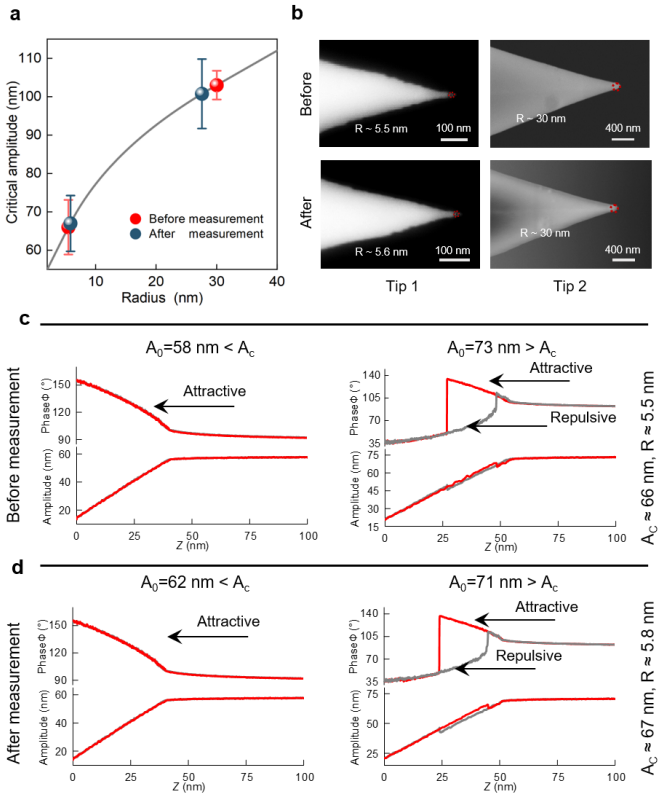

Supplementary Figure 8. In-situ determination of tip radius by critical amplitude method.

a, The change in tip critical amplitude (A_c) and the corresponding tips radius (AN-CSG01) after performing 300 force curves. Error bars represent the mean deviation. **b,** SEM images of the two tips in **a**. **c, d,** Experimental amplitude and phase distance (APD) curves recorded for different values of free amplitude A_0, acquired before and after the execution of the 300 force curves.

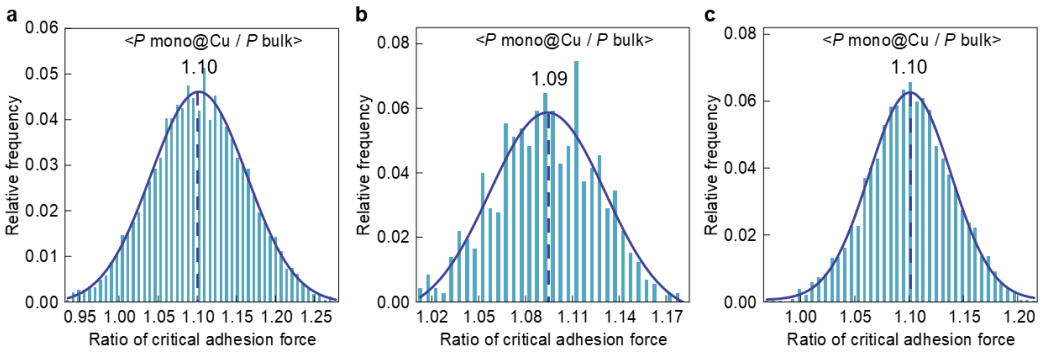

Supplementary Figure 9. The stability of force measurements using diamond-like-carbon coated tips.

a, b, c, Histograms distribution of $P_{mono@Cu}/P_{bulk}$ ratio. The solid lines are Gaussian fits. The standard deviations are 0.061, 0.037 and 0.038, respectively.

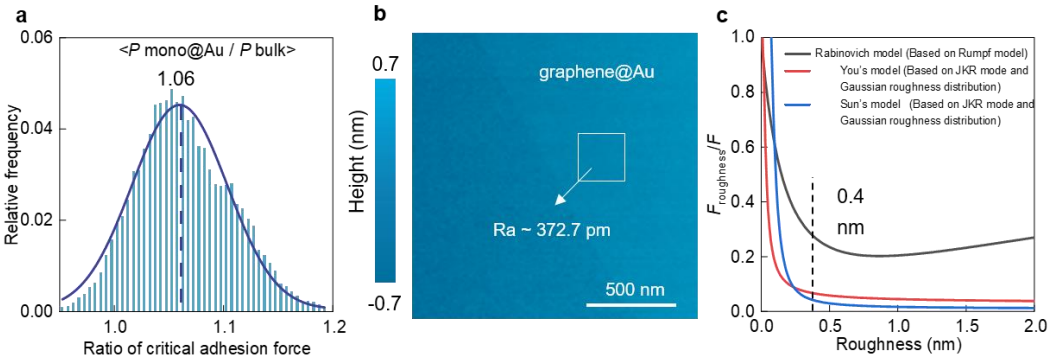

Supplementary Figure 10. The vdW contribution from Au substrates.

a, Histogram distribution of $P_{mono@Au}/P_{bulk}$ ratio. The solid line is Gaussian fit. The standard deviation is 0.044. **b,** Roughness of graphene on the Au is around 0.4 nm. The white line denotes scale bar, 500 nm. **c,** Roughness adhesion model. $F_{roughness}/F$ is the ratio of adhesion on tip-sample (rough) and tip-sample (smooth).

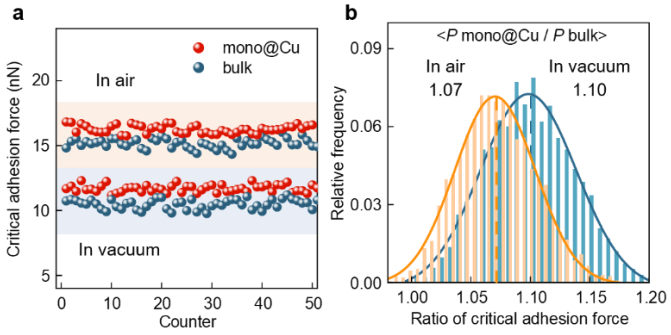

Supplementary Figure 11. Surface adhesion of sample measured in vacuum and ambient.

a, Critical adhesive force detected on mono@Cu and bulk graphite in air (orange shaded region) and vacuum (blue shaded region). **b,** Histograms distribution of $P_{\text{mono@Cu}}/P_{\text{bulk}}$ measured in air (orange) and vacuum (blue). The solid lines are Gaussian fits. The standard deviations are 0.034 and 0.040, respectively.

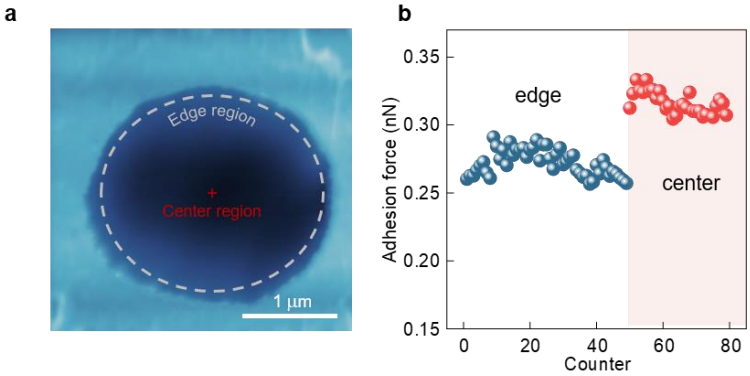

Supplementary Figure 12. Elastic deformation contribution to the critical adhesion force on the suspended graphene.

a, AFM topography of graphene suspended over a graphite hole with a diameter of 2.5 μm. Scale bar, 1 μm. **b,** Distribution of critical adhesion force measured at the hole center and ~100 nm away from the hole edge.

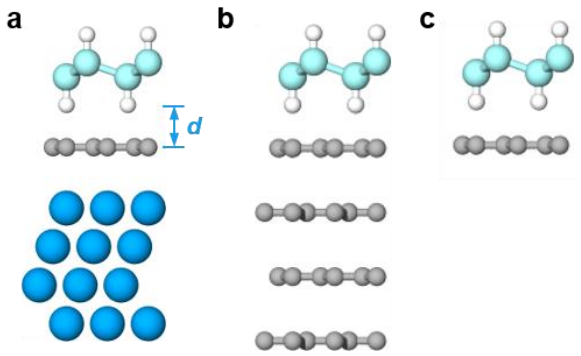

Supplementary Figure 13. Atomic structures of the heterogeneous interfaces used in the density function theory (DFT) calculations.

a, Si-mono@Cu. **b,** Si-bulk graphite. **c,** Si-monolayer graphene.

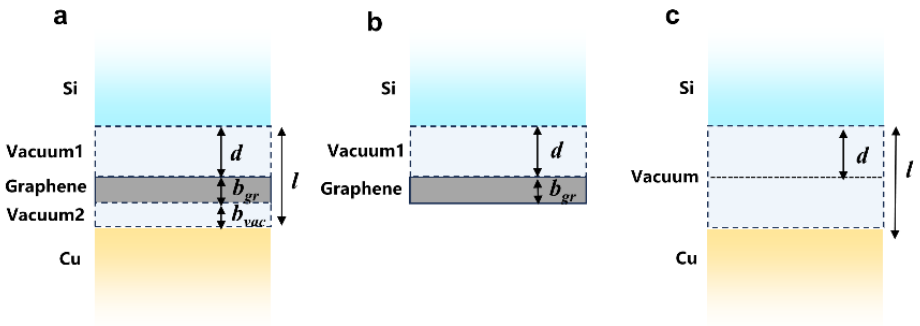

Supplementary Figure 14. Illustration of models used in the Lifshitz theory for the qualitative understanding of the vdW screening effect.

a, Model used to calculate the vdW energy between semi-infinite silicon and graphene supported by semi-infinite Cu substrate. **b,** Model used to calculate the vdW energy between silicon and monolayer graphene. **c,** Model used to calculate the vdW energy between silicon and Cu substrate.

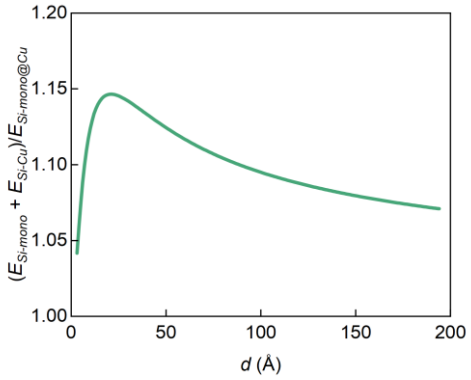

Supplementary Figure 15. Ratio of $E_{Si\text{-}mono}+E_{Si\text{-}Cu}$ to $E_{Si\text{-}mono@Cu}$ as a function of interlayer separation predicted by Lifshitz theory.

Element	C_6 (applied)	C_6 (free atom)
C	17.63	12.0
Cu	125.47	253.0
Si	166.0	305.0

Supplementary Table 1. C_6 coefficients (in unit of Hartree·bohr^6) of the pairwise vdW correction.

Supplementary References

1. Hao, Y. et al. Probing layer number and stacking order of few-layer graphene by raman spectroscopy. *Small* **6**, 195 (2010).
2. Goossens, A. et al. Mechanical cleaning of graphene. *Appl. Phys. Lett.* **100**, 073110 (2012).
3. Sader, J. E. & Jarvis, S. P. Accurate formulas for interaction force and energy in frequency modulation force spectroscopy. *Appl. Phys. Lett.* **84**, 1801 (2004).
4. Katan, A. J., Van Es, M. H. & Oosterkamp, T. H. Quantitative force versus distance measurements in amplitude modulation AFM: a novel force inversion technique. *Nanotechnology* **20**, 165703 (2009).
5. Ramakrishna, S. N., Clasohm, L. Y., Rao, A. & Spencer, N. D. Controlling adhesion force by means of nanoscale surface roughness. *Langmuir* **27**, 9972 (2011).
6. Jiang, T. & Zhu, Y. Measuring graphene adhesion using atomic force microscopy with a microsphere tip. *Nanoscale* **7**, 10760 (2015).
7. Rabinovich, Y. I. et al. Adhesion between nanoscale rough surfaces: I. Role of asperity geometry. *J. Colloid Interface Sci.* **232**, 10 (2000).
8. You, S. & Wan, M. P. Mathematical models for the van der Waals force and capillary force between a rough particle and surface. *Langmuir* **29**, 9104 (2013).
9. Sun, Q., Peng, W. & Hai, X. Mathematical model and atomic force microscopy measurements of adhesion between graphite particles and rough walls. *Appl. Surf. Sci.* **562**, 149976 (2021).
10. Tkatchenko, A. & Scheffler, M. Accurate molecular van der Waals interactions from ground-state electron density and free-atom reference data. *Phys. Rev. Lett.* **102**, 073005 (2009).
11. Liu, X. Yang, J. & Guo, W. Semiempirical van der Waals method for two-dimensional materials with incorporated dielectric functions. *Phys. Rev. B* **101**, 045428 (2020).
12. Zhang, G. X., Tkatchenko, A., Paier, J., Appel, H. & Scheffler, M. Van der Waals interactions in ionic and semiconductor solids. *Phys. Rev. Lett.* **107**, 245501 (2011).
13. Bentsen, V. S., Herikstad, R., Skriudalen, S., Brevik, I. & Høye, J. S. Calculation of the Casimir force between similar and dissimilar metal plates at finite temperature. *J. Phys. A: Math. Gen.* **38**, 9575 (2005).
14. Rakić, A. D., Djurišsić, A. B., Elazar, J. M. & Majewski, M. L. Optical properties of metallic films for vertical-cavity optoelectronic devices. *Appl. Opt.* **37**, 5271 (1998).
15. Tkatchenko, A., Ambrosetti, A. & DiStasio, R. A. Interatomic methods for the dispersion energy derived from the adiabatic connection fluctuation-dissipation theorem. *J. Chem. Phys.* **138**, 074106 (2013).
16. Tkatchenko, A., DiStasio, R. A., Car, R. & Scheffler, M. Accurate and efficient method for many-body van der Waals interactions. *Phys. Rev. Lett.* **108**, 236402 (2012).
17. Khomyakov, P. A. et al. First-principles study of the interaction and charge transfer between graphene and metals. *Phys. Rev. B* **79**, 195425 (2009).
18. Taft, E. A. & Philipp, H. R. Optical properties of graphite. *Phys. Rev.* **138**, A197 (1965).
19. Palik, E. D. & Ghosh, G. *Handbook of Optical Constants of Solids*. (Academic Press, 1998).
20. Jiang, Z. et al. Large Casimir flipping torque in quantum trap. *J. Phys. Chem. Lett.* **128**, 350 (2023).
21. Parsegian, V. A., *Van der Waals forces: a handbook for biologists, chemists, engineers, and*

physicists. (Cambridge university press, 2005).